Macromolecular Materials and Engineering
www.mme-journal.de

Wire Melt Electrospinning of Thin Polymeric Fibers via Strong Electrostatic Field Gradients

*Kai Morikawa, Aniruddh Vashisth, Christian J. Grimme, Micah J. Green, and Mohammad Naraghi**

Here, a novel melt electrospinning method to produce few-micron and nanometer thick fibers is presented, in which a polymer-coated wire with a sharp tip is used as the polymer source. The polymer coating is melted via Joule heating of the source wire and extracted toward the target via electrostatic forces. The high viscosity and low charge density of polymer melts lower their stretchability in melt. The method relies on confining the Taylor cone and reducing initial jet diameter via concentrated electrostatic fields as a means to reduce the diameter of fibers. As a result, the initial jet diameter and the final fiber diameter are reduced by an order of magnitude of three to ten times, respectively, using wire melt electrospinning compared to syringe- and edge-based electrospinning. The fiber diameter melt electrospun via this novel method is 1.0 ± 0.9 µm, considerably thinner than conventional melt electrospinning techniques. The generation of thin fibers are explained in terms of the electrostatic field around the wire tip, as obtained from finite element analysis (FEA), which controls the size and shape of the melt electrospun jet.

1. Introduction

Few-micron and sub-micron thick polymer fibers are being used and considered for use in many applications including wound healing, additive manufacturing filtration, and energy storage.[1–7] Moreover, they can be used as precursors for non-polymeric nanofibers such as carbon nanofibers, which find use in composites in automotive and aerospace industries.[8–10] These low-diameter polymer fibers are useful because of characteristics such as high surface to volume ratio, a mere effect of their small diameter, and in many cases enhanced material properties such as strength and toughness compared to the same polymer in bulk form.[11–15] Despite all the potential benefits of low-micron and sub-micron polymer fibers, scalable processing methods of polymer fibers with such low diameter is still in its infancy.

Various methods have been developed to fabricate nanofibers in large quantities by incorporating multiple needles and edge electrospinning.[16,17] In these methods, a polymer is often dissolved in a solvent, and the solution is ejected at a specific rate out of a spinneret via electrostatic forces. While solution electrospinning is commonly used to fabricate polymer nanofibers, it requires solvents up to 5–50 times the mass of produced nanofibers.[1,18,19] The large quantity of solvent (relative to the polymer) required to achieve sufficiently low viscosity for solution electrospinning increases the fabrication costs of nanofibers. Moreover, the solvents used are often toxic and the environmental footprint left from solvent evaporation can be highly unattractive for industrial-scale production.[20–22] Also, the presence of residual solvent in the as-spun product can become a barrier for entry to market in certain applications, such as water filtration, requiring post-electrospinning modifications to extract the residual solvent.

As an alternative process to solution electrospinning for fabrication of thin polymeric fibers, melt electrospinning can be used. Melt electrospinning eliminates the challenges associated with using solvents. The forces used to drive the jet in this process are electrostatic, the same as solution electrospinning, but in melt electrospinning, the polymer is drawn in the melted state, rather than in solution phase (**Figure 1**). This solvent-free method typically produces fibers mostly with diameters of tens of microns or more, which is considerably thicker than solution electrospinning with typically sub-micron fibers.[23–30] The larger diameter of fibers obtained with melt spinning is caused by several factors. First, the charge density of polymer melt is low, and its viscosity is high, relative to polymer solution.[31–33] The lower charge density results in a lower electrostatic force applied on the jet and is generally insufficient to reduce jet diameter to below a micron. The high viscosity of the melt also makes it more difficult for the electrostatic field to draw the jet.

K. Morikawa, Dr. A. Vashisth, Prof. M. Naraghi
Department of Aerospace Engineering
Texas A&M University
3409 TAMU, College Station
TX 77843-3409, USA
E-mail: naraghi@tamu.edu
C. J. Grimme
Department of Macromolecular Science and Engineering
Case Western Reserve University
Cleveland, OH 44106-7202, USA
Prof. M. J. Green
Artie McFerrin Department of Chemical Engineering
Texas A&M University
3122 TAMU, College Station
TX 77843-3122, USA
The ORCID identification number(s) for the author(s) of this article can be found under https://doi.org/10.1002/mame.201800417.

DOI: 10.1002/mame.201800417

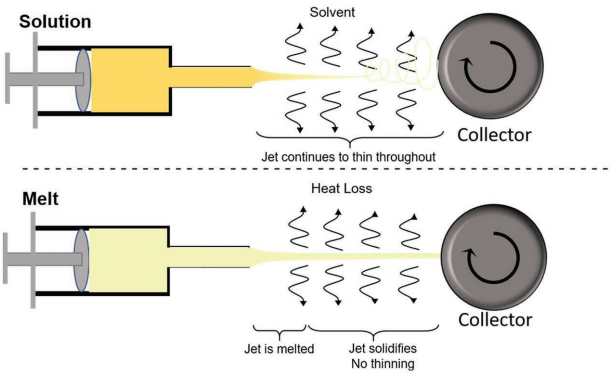

Figure 1. Schematic demonstrating fundamental differences between solution and melt electrospinning.

Additionally, melt electrospinning must be carried out in temperatures lower than the melting temperature of the polymer, so the heat exchange due to convection can solidify the jet. This often confines the thinning of the jet to a region in the vicinity of the Taylor cone where the jet is still in the melted state. Since the heat loss occurs on the surface of the jet (interface of the jet with air), the heat loss to the environment increases as additional thinning occurs due to the increased surface area to volume ratio of the jet.[34–36]

Theoretically, one may use smaller needles to achieve small fibers via syringe melt electrospinning. However, reducing the needle diameter (R) is not an effective strategy, since it will drastically increase the pressure drop (ΔP) along the needle ($\Delta P \propto R^{-4}$). Other modifications to the process have also been attempted by researchers, such as the use of downstream heating to increase the region that the jet stays in the melted, and thus stretchable state,[34,37] and the addition of conductive nanoparticles to increase the charge density of the melt.[38,39] However, as the rate of heat loss from the polymer jet to the surrounding environment is proportional to the surface to volume ratio of the polymer (i.e., inversely proportional to the jet diameter), smaller diameters require higher input power. As the diameter of the jet is reduced to a few microns, the input heat required to counter the heat loss effectively becomes excessively large.[34] Moreover, the addition of nanoparticles may limit the applications of the processed fibers due to undesired changes in properties of the polymer as well as increased viscosity.[40]

In light of the above opportunities and challenges, a remedy to reduce the diameter of melt electrospun fibers can be sought by lowering the initial diameter of the jet (i.e., the Taylor cone size), or simple geometrical confinement of the jet. Given the unfavorable scaling of the pressures required to push a polymer melt through a needle with the needle diameter (governed by Hagen–Poiseuille law), the jet confinement will be effective only if successfully implemented without physical walls. This approach is partly motivated by prior studies which suggest a direct correlation between the initial jet diameter and the diameter of the melt electrospun fibers.[34–36]

The objective of this study is to reduce the fiber diameter by confining the initial diameter of the Taylor cone and the polymer jet in melt electrospinning. This is achieved by changing the geometry of the spinneret which in turn changes the distribution of the electrostatic field driving the jet. We initiate strong field gradients that can assist in overcoming the surface tension of the electrospinning fluid locally and lead to the flow of a geometrically confined jet. Due to the confinements by the electric field, the polymer jet forms a much smaller Taylor cone thereby forming fibers with smaller diameters as compared to previous melt electrospinning configurations using the same overall processing parameters.

2. Experimental Methods

Polycaprolactone (PCL; 14000 Mw, Sigma-Aldrich Co.) was used as bought in this study. A high voltage power supply (Acopian, N030HP1) was used to provide the electric field. The fibers were collected on a rotary target. For syringe electrospinning, 14-gage needle (stainless steel, McMaster Carr) was used. The polymer was heated in a 10 mL syringe, heated using a syringe heater (New Era Pump Systems, HEATER-KIT-1LG), and pumped using a syringe pump (New Era Pump Systems, NE-1000). For edge electrospinning, a 15×15 cm^2, 1 cm thick aluminum sheet, with a 45° taper angle was used. For wire electrospinning, nickel chromium wire of various thickness (200, 500, 1000 μm) was used as the source wire. A 200 μm nickel chromium wire was wrapped around the source wire to provide Joule heating. The current through the Joule-heating wire varied to keep a constant temperature of the main wire. Figure 1 shows a schematic for the various electrospinning configurations studied in this work. In all these cases, the right side of the figure shows the rotary disk, while the left side is the source of the polymer.

The electrospinning parameters were as follows for all cases: temperature of the polymer source (syringe, flat plate, and wire) was set at 100 °C, electrospinning distance was set to 5 cm, and the collector speed was set at 270 RPM (≈2.9 m s^{-1}). The electrospinning voltage was kept at the lowest possible voltage required to generate a stable jet in all configurations of the source (syringe, edge, and wire melt electrospinning).

For syringe melt electrospinning, the flow rate was set to be the same as the flow rate of a stable jet formed from wire melt electrospinning. This was calculated using the average fiber diameter of wire melt electrospun fibers as well as the tip velocity of the collector.

To image the Taylor cone during electrospinning, a CCD camera (EO USB 2.0 CCD) with a zoom imaging lens (VZM 450 zoom imaging lens) and extender lens (VZM 4500.53 extender lens) was used. An optical microscope (Olympus SZX16) was used to image the collected fibers, which were analyzed using ImageJ. Fibers were sputtered with 10 nm thick iridium coating and imaged using FEI Quanta 600 FE-SEM. Crystallinity measurements on electrospun fibers and as-received PCL were carried out using differential scanning calorimetry (DSC). A temperature scan over a range of 20–80 °C at 10 °C min^{-1} was carried out using a Pyris 1 DSC (PerkinElmer Instruments) machine. For each run, 3–4 mg of sample was used.

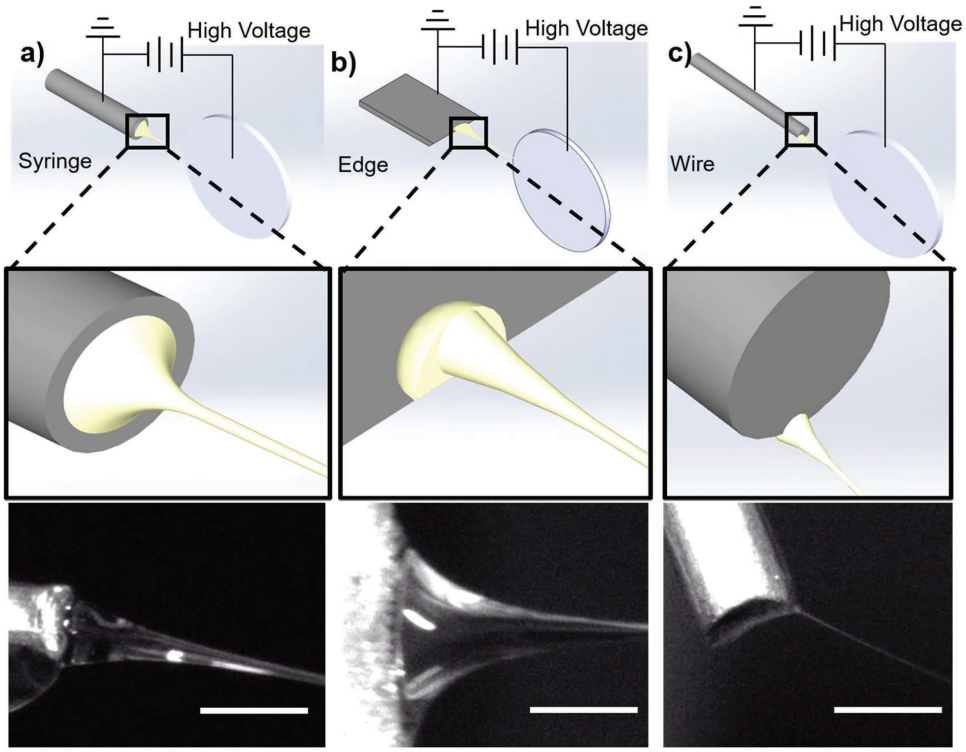

Figure 2. Schematic and Taylor cone images for various melt electrospinning methods: a) syringe, b) edge, and c) wire melt electrospinning. The Taylor cone images have been post-processed to better display the jet. The schematics are roughly drawn to scale. In the schematics, grey is the spinneret and yellow is the polymer melt, and the white disk is the collector. All scale bars are 1 mm.

3. Results and Discussion

3.1. Effect of Spinneret Architecture on Size of the Jet and Fiber Diameter

In conventional melt electrospinning, the polymer melt is supplied through a needle or at the edge of a flat "source plate" and drawn via electrostatic forces into fibers.[41–44] In this investigation, we have introduced a novel spinneret geometry to drastically confine the jet initiation zone as a means to achieve much smaller initial jet diameter. Our electrospinning setup to spin fibers consists of a wire which is coated with a polymer (source wire), thus, it is referred to as "Wire Melt Electrospinning." The polymer studied here was PCL due to its relatively low melting point (≈60 °C). Since the melting point of PCL is significantly lower than its degradation temperature (≈150 °C), PCL provides a wide temperature range for melt electrospinning. The PCL coated on the source wire is melted via Joule heating. We do so by passing a current through a coil which is wrapped around the wire.

To initiate the fiber spinning, an electrostatic voltage was applied between the source wire and target as shown in **Figure 2**. The wire has a sharp tip to induce highly concentrated electrostatic fields which initiate the electrospinning jet in small region at the wire tip and confine the Taylor cone. This approach to induce a flow of a polymer melt is driven by prior studies in patterning polymers via concentrated electrostatic fields in which locally strong electrostatic forces can overcome the surface tension and generate a local flow normal to the initially undisturbed (prior to flow) polymer surface.[45,46]

The wire melt electrospinning setup is shown in Figure 2c schematically alongside the conventional melt electrospinning setups, that is, edge and syringe melt electrospinning in Figure 2b and a, respectively. Under the schematics are representative images of the Taylor cone for each configuration. The schematics are drawn to scale. The inset below each configuration is an optical image of the Tylor cone and the polymer jet for respective electrospinning method. In all experimental cases, the applied voltage is kept at the minimum required to achieve continuous melt electrospinning. As shown in Figure 2, the jet formed in the syringe and edge melt electrospinning is much thicker than the jet generated in our method (wire melt electrospinning).

In syringe melt electrospinning, the initial jet diameter (roughly taken to be the size of the Taylor cone) is dictated by the needle's inner diameter as shown in Figure 2a. Moreover, the polymer melt in edge electrospinning is allowed to spread along the edge of the flat plate, and the initial jet diameter is comparable to that of the polymer in syringe electrospinning. In edge electrospinning, initial jet diameter is determined by a competition between the surface tension of the melted polymer, adhesion between the polymer and the spinneret, and the electrostatic forces applied to the jet.

We studied the fiber diameter obtained from the melt electrospinning setups (syringe, edge, and wire melt electrospinning) as reported in **Figure 3**a. It is to be noted that all other melt electrospinning parameters, such as polymer type, electrospinning temperature, remained the same. The only exception was the applied voltage, which as stated earlier, in all cases was

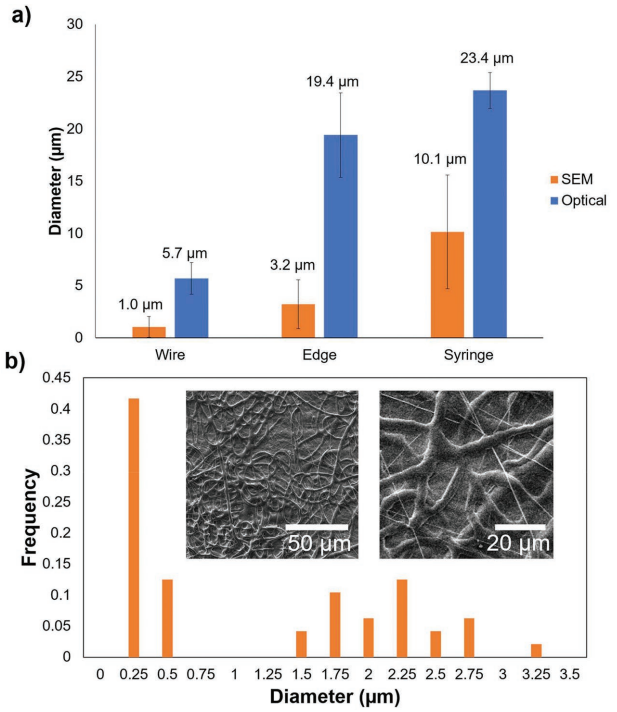

Figure 3. a) Fiber diameter for various electrospinning methods (data labels are average diameters), and b) diameter distribution of wire melt electrospun fibers measured using scanning electron microscopy (inset is SEM image).

kept as the minimum voltage required to carry out uninterrupted melt electrospinning. This voltage was in the range of 15–17 kV.

We obtained the diameter through optical and scanning electron microscopy (SEM) methods. From SEM images, the diameter of the wire melt electrospun fibers was measured to be 1.0 ± 0.9 μm which is ≈10 and ≈3.2 times thinner than the fibers obtained from syringe electrospinning (diameter of 10.1 ± 5.4 μm) and edge electrospinning (diameter 3.2 ± 2.3 μm), respectively. Optical imaging also confirms the formation of considerably thinner fibers via wire-based melt electrospinning (5.7 ± 1.5 μm vs 23.7 ± 1.7 μm and 19.4 ± 4.0 μm for syringe and edge electrospinning, respectively). The diameter distribution as measured from SEM images appears to be bimodal, as seen in Figure 3b. This bimodal distribution of fiber diameters has been reported in previous studies and can be attributed to jet splitting downstream of the spinneret. Alternatively, thinner fibers can form as a result of the extension of molten droplets which get separated from the source due to electrostatic forces.[47,48] More studies are being carried out to more vigorously explain the formation of the thinner fibers, and if possible, to suppress the formation of the thicker fibers in favor of the thinner fibers for applications where polymeric nanofibers are more sought. Diameter distribution plots for wire, edge, and syringe electrospun fibers for SEM and optical techniques can be found in Figures S1–S3, Supporting Information, respectively.

The low fiber diameter distribution correlates well with the small initial jet diameter; such a correlation between fiber diameter and initial jet diameter has been alluded to in previous studies.[34] However, the most interesting part of this study is the drastic reduction in the initial jet diameter, especially when comparing with the two needle-less methods (edge and wire melt electrospinning), which leads to thinner fibers in wire-based methods by a factor of 3–10. This approach to confine the jet as a means to form considerably thinner fibers is unprecedented in the literature.

It is, however, to be noted that the initial jet diameter was ten times smaller in wire electrospinning compared to the other two methods, while the reduction in fiber diameter is more modest. That is because reducing the jet diameter in wire melt electrospinning increases its surface to volume ratio, which increases the heat loss from the jet, leading to the solidification of the jet within a shorter distance from the Taylor cone.

3.2. Effect of Wire Diameter on Fiber Diameter

Further experiments on wire melt electrospinning with various wire diameters were carried out to elucidate the mechanism of fiber diameter reduction. Given that the wire diameter can influence the electric field intensity especially near the wire tip, we experimentally studied the dependence of wire diameter (200, 500, and 1000 μm) on final fiber diameter. Although we observed slight variations of the fiber diameter among different cases, the fiber diameter in all cases was in the range of 5–7 μm. Within the experimental uncertainty, the wire diameter does not have a noticeable effect on fiber diameter, as shown in **Figure 4**. The diameter measurements for the various runs of the above experiments can be found in Figure S4, Supporting Information.

Thus, we hypothesize that the confinement of the jet is primarily driven by the distribution of the electrostatic field around the tip of the wire, which induces localized electrostatic forces on the melted polymer coating. The electrostatic forces can overcome the surface tension and form a Taylor cone only in a narrow region around the wire tip. This hypothesis is in line with the observation that the polymer jet forms only at the tip of the wire.

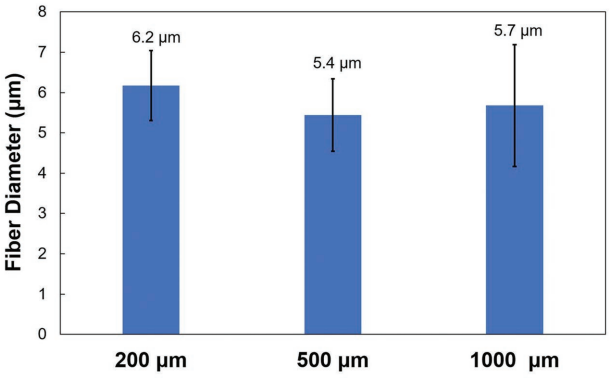

Figure 4. Fiber diameter dependence on wire diameter (data labels are average diameters).

To further illustrate the validity of this hypothesis, we modeled the distribution of the electric field that the polymer jet experiences using COMSOL Multiphysics Software (Finite Element Analysis). The simulation was carried out by using the electrostatics model which solves the Laplace equation, using a 2D axisymmetric space dimension. The electrostatic potential difference between the collector and the polymer source was set to be 15 kV with a spinning distance of 5 cm. Each geometry of the simulation was given a width of 100 μm to reliably simulate experimental conditions. Note that no polymer was present in the model in most cases, but the insertion of a 100 μm thick coating of a dielectric material with properties of PCL on the spinneret did not affect the results significantly (less than 1% change in electric field strength).

The electric field intensity as a function of the distance from the center of the jet is shown in **Figure 5**. For the case of syringe electrospinning, the center of the jet is at the center of the needle, and in the case of wire, the center of the jet is the sharp tip of the wire. The electric field is normalized by the average electric field between the spinneret and collector, which is the same in all cases. For each case, we have also identified the region from which polymer jet is initiated in the experiments. This region is shown in the schematic above each plot in Figure 5.

In wire electrospinning, the electric field reaches its maximum value at the tip of the wire, where the local curvature of the source wire is the highest (Figure 5a). That is where the coating is sufficiently charged to overcome the surface tension, and the jet is initiated in the experiments. It is interesting to note the significant concentration of the electrostatic field at the corner of the wire, which can reach values as high as 60 times the average electrostatic field intensity (equal to the applied voltage divided by the distance from the spinneret to collector). In the vicinity of wire tip at a lateral distance of only ≈100 μm, the electrostatic field drops by half and will not be strong enough to overcome the surface tension. Thus, the Taylor cone is confined to the tip of the wire due to the weak electric field elsewhere.

A comparison of the electrostatic fields around the spinneret between syringe and wire melt electrospinning will more clearly demonstrate the role of electrostatic field distribution and geometry of the spinneret in generating thin jets. The syringe melt electrospinning can be approximated as an axisymmetric process with respect to the axis of the needle, and the center of the jet coincides with the syringe axis as shown in Figure 5b. Thus, we presented the relative electrostatic field as a function of the radial distance from the axis of the needle. In the case of syringe electrospinning, the electrostatic field intensity on the walls of the syringe is approximately four times stronger than the electric field intensity at the center of the syringe, as shown in Figure 5b. However, in syringe electrospinning, the jet does not form from the outer edge of the needle where the local electrostatic field is the strongest. Instead the Taylor cone spans the entire cross-section of the needle. The Taylor cone forms as a result of the competition between two forces acting at its periphery: surface tension force, and electrostatic force ($\overrightarrow{F_S}$ and $\overrightarrow{F_E}$ respectively, in Figure 5b). The surface tension force acts normal to the jet, and electrostatic force drives the jet toward the collector.[49] The resultant of these forces ($\overrightarrow{F_R}$) is in the direction of the flow, leading to the formation of the large jet.

The formation of fibers that are several times thinner in wire melt electrospinning compared to edge and syringe melt electrospinning methods can be attributed to the size of the Taylor cone in the plane normal to the jet, which depends on how well the jet is confined on the spinneret via physical walls or other means. For instance, in syringe melt electrospinning, the Taylor cone will spread radially (normal to the flow direction) approximately all the way to the inner wall of the needle. Thus, the jet is confined via physical boundaries. In the setups used in this study, the lateral dimensions of the Taylor cone formed at the tip of the needle is ≈1 mm, which is five to ten times larger than the lateral dimensions of the Taylor cone in wire melt electrospinning method (Figure 2). Hence, relatively speaking, one may refer to conventional syringe and wire electrospinning respectively as 2D and 0D approaches, where 2 and 0 refer to the number of orthogonal dimensions in the lateral direction (transverse to the jet) that the jet is allowed to spread until it reaches a confining boundary, that is, either physical walls (syringe) or electrostatic (wire) confinement. One may reduce the size of the Taylor cone in syringe melt electrospinning by employing needles with smaller inner diameters as a means to better confine the jet.[35] However, according to Hagen–Poiseuille law in fluid dynamics of laminar flows, this is highly disadvantageous as the pressure required to maintain a certain flow of melted polymer within the needle increases with the relation $\Delta P \propto R^{-4}$. Following the same arguments, the edge melt electrospinning can be approximated as a 1D approach, since the jet is allowed to spread in one dimension, that is, along the edge of the plate. However, according to the results presented in the previous section, the competition between the electrostatic forces and surface tension eventually leads to a Taylor cone that is significantly wider (five to ten times) than the one obtained in the wire melt electrospinning. In other words, this type of jet confinement, similar to the syringe approach, is not very useful in reducing the fiber diameter when compared to the wire method. Hence, it seems that it is the largest dimension in the spinneret geometry (in the plane normal to the flow) which confine the Taylor cone, and controls the initial jet diameter and the final fiber diameter.

3.3. Continuous Electrospinning from Tip of Wire

Continuous or nearly continuous melt electrospinning relies on our ability to control the coating thickness and Taylor cone during electrospinning and prior to that when coating the wire. Unlike conventional syringe melt electrospinning in which the melt is supplied continuously from a reservoir, the coating in our method will in principle be gradually depleted, which can interrupt the process. To study the continuity of electrospinning in our approach, we monitored the coating thickness and the initial jet diameter as a function of the electrospinning time. The variation of coating thickness and the corresponding changes of the initial jet diameter with time is shown in **Figures 6** and **7**, respectively. As shown in Figure 6, the coating becomes thinner with the progression of melt electrospinning, as expected from the conservation of mass principle. However, the rate of thickness reduction slows down with time, until the coating thickness reaches a value of 74 ± 19 μm, which we refer

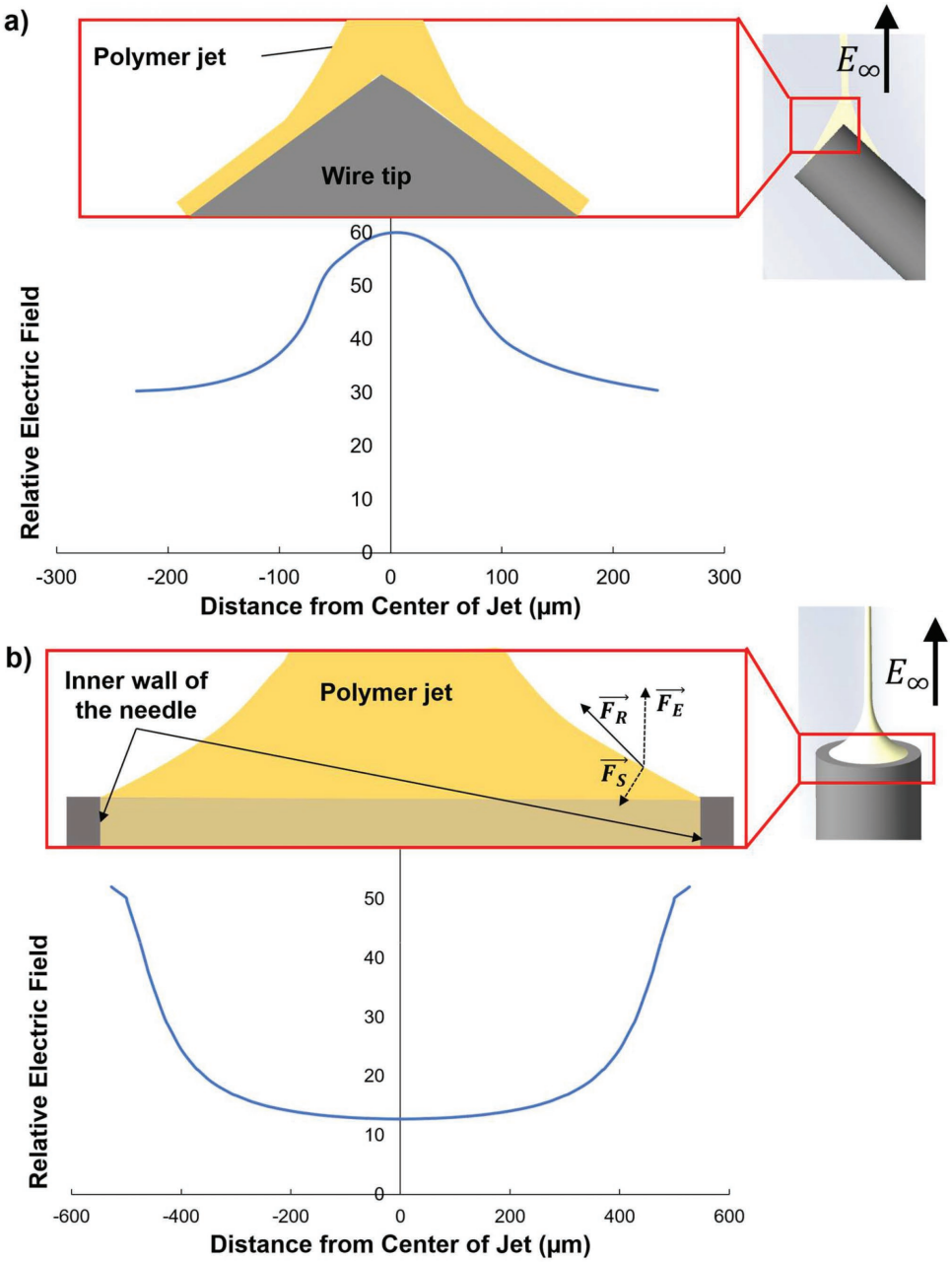

Figure 5. Relative electric field as a function of distance from center of jet for a) wire electrospinning and b) syringe electrospinning. Above each plot is a schematic of the Taylor cone and the location it is observed. Forces in (b) are F_E (electric field force), F_S (surface tension force), and F_R (resultant force).

to as the stable coating thickness. It is interesting to note that in multiple repetitions of the experiments with various initial coating thickness values, the coating reached similar stable thicknesses.

The stable coating thickness can be explained in terms of a competition between two flow rates: i) the flow of the polymer away from the tip of the wire in the form of the electrospinning jet and ii) the flow of the polymer melt along the wire towards the tip (upstream of the wire tip). The formation of the Taylor cone is driven by the locally concentrated electrostatic fields at the wire tip in competition with the surface tension of the polymer, as discussed in the previous sections. Moreover, no polymer flow was observed along the wire in the absence of the electrostatic field, suggesting a negligible contribution of gravity to the flow of the polymer melt along the wire. Thus, the electrostatic field seems to be the major contributor to both flows. More specifically, the component of the electrostatic field which is tangential to the wire surface is the main contributor to the flow along the wire.

The accumulation of polymer melt at the tip of the wire, as shown in the early stages of wire melt electrospinning (e.g., Figure 6a), is likely an indication that the flow rate of the polymer along the wire (flow rate ii) is initially higher than the jet flow rate (flow rate i). On the other hand, the flow of the jet reduces the coating thickness due to the conservation of mass,

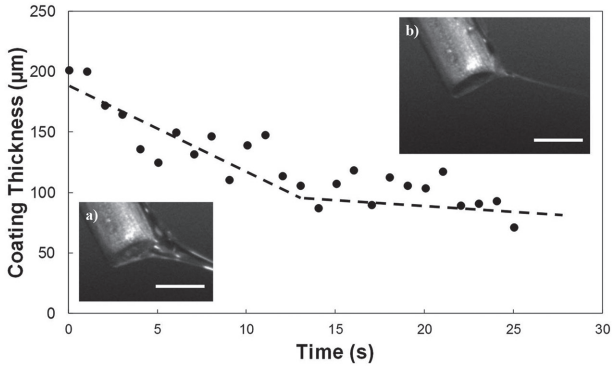

Figure 6. Coating thickness as a function of time. Images represent coating and jet geometry at various times, at a) 2 s and b) 18 s. All scale bars are 1 mm.

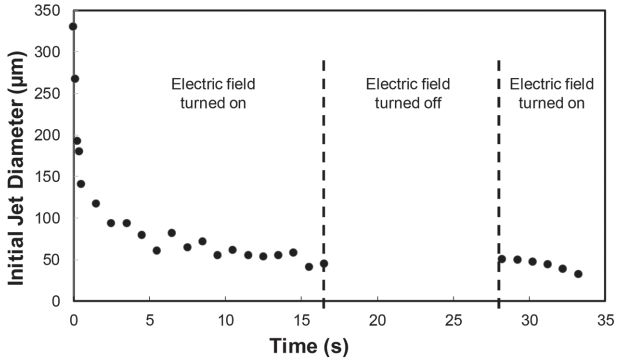

Figure 7. Initial jet diameter as a function of time. Middle region has no electric field.

resulting in a reduction in the flow rate along the wire (flow rate ii). That is because the tangential component of the electrostatic field experienced by the coating which drives upstream flow diminishes as the surface of the coating approaches the surface of the wire (note that the electrostatic field is perpendicular to the conductive wire surface). The stable coating thickness forms when the upstream flow rate becomes equal to (i.e., is reduced to the magnitude of) the jet flow rate. It is, however, to be emphasized that this stable coating thickness does not last in perpetuity, and the electrospinning stops due to sufficient mass loss.

The variation of the size of the Taylor cone with time provided more evidence in support of the above discussion and the consideration of two flows. For instance, a comparison between the variation of the coating thickness and Taylor cone with time (Figures 6 and 7, respectively), reveals that the Taylor cone reaches a stable size much faster than the coating thickness, that is, the Taylor cone reaches the stable thickness in less than ≈5 s, while the stable thickness of coating is reached within ≈20 s in the particular case shown in the figures. In other words, there is no correlation between the time required for reaching stable flow in the upstream of the wire tip and at the wire tip. Moreover, the fact that the Taylor cone reaches a stable size regardless of the coating thickness demonstrates the effectiveness of the wire melt electrospinning.

We also studied the formation of the Taylor cone and melt electrospinning subjected to deliberate interruptions by turning off the voltage and back on, as shown in Figure 7. In this experiment, the voltage was turned off after the stable coating thickness was achieved. When the electric field is turned back on, the jet immediately resumes. Figure 7 demonstrates that if wires are prepared with the correct coating thickness, the large Taylor cone that is observed initially can be avoided completely. This is significant for scalability purposes. If coating of specified thicknesses are prepared by certain means, the process can be scaled up with multiple coated wires to get an increase in fiber throughput. A concept to scale-up the wire-based melt electrospinning is presented in Figures S5 and S6, Supporting Information. This can, for instance, be achieved by coating the wires via dipping, as presented in the Supporting Information. Ideally, the unstable regime of electrospinning can become nonexistent by simply starting with a source wire that has a coating thickness equal to the stable coating thickness.

3.4. Effect of Spinneret Architecture on Crystallinity

DSC thermo-analysis was carried out to determine the crystallinity of fibers manufactured using different techniques. **Figure 8** shows the DSC curve for various melt electrospun fibers as well as as-received PCL. The melting peak occurs around 60 °C for all the melt electrospun samples which was slightly lower than the as-received powder.[50] The slightly lower melting point of the electrospun samples might be an indication of slight thermal degradation that PCL has experienced during electrospinning due to Joule heating. Moreover, the nonhomogeneous cooling of the jet stream results in heterogeneous nucleation[51] of the polymer crystals that causes melting peak to have a small shoulder that was not observed in as-received powder.

The crystallinity was calculated by measuring the melting enthalpy and comparing that with the melting enthalpy of 100% crystalline PCL, as reported in the literature.[52] In general, the degree of crystallinity as the polymer melt cools down below the melting point during electrospinning due to convective heat loss may depend on the cooling rate experienced by the polymer.[53] Faster cooling rates reduce the time that crystals

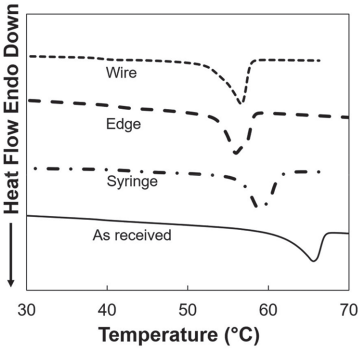

Method	Crystallinity (%)
Wire	52 ± 16
Edge	46 ± 16
Syringe	51 ± 9
As received	43 ± 15

Figure 8. DSC curves for differing spinneret architectures (left) and table of crystallinity values (right).

are allowed to form, and it may lead to reduced crystallinity. Thus, thinner fibers might be at a disadvantage due to their higher surface to volume ratio which increases the rate of heat loss. On the other hand, the crystallinity of fibers fabricated with the three methods are comparable within the experimental uncertainties (46–52%). This is despite the fact that wire melt electrospun samples were several times thinner than the fibers fabricated via other melt electrospinning method. Hence, we conclude that the time associated with the formation of crystals were significantly lower than the duration of the flight of the jet (in the order of tens of milliseconds), and the crystallinity achieved in all samples was limited by the loss of mobility of the amorphous segments of the chains which were partly anchored within the already formed crystalline domains.

4. Conclusion

We demonstrated a novel melt electrospinning technique in which modified spinneret geometries allow for a reduction in Taylor cone size caused by concentrated electric field. Given the high viscosity and low charge density of typical polymer melts, the focus of our method was to initiate thinner jets as a means to generate thinner fibers. This is drastically different from conventional melt electrospinning methods (e.g., syringe or edge melt electrospinning) which have often relied on jet drawing via electrostatic forces combined with enhancing the jet stretchability (e.g., by adding plasticizers or heating the jet) to generate thin fibers, with limited success. The method developed in this investigation allows for the production of fibers with a significantly lower diameter (average of 1 μm) and higher specific surface area, especially when compared to fibers obtained by conventional melt electrospinning such as syringe and edge melt electrospinning.

The novelty of our work is the geometry of the polymer source, that is, the wire, which despite its simplicity, applies a highly concentrated electrostatic field to the polymer coating. The concentration of the electrostatic field confines the size of the generated Taylor cone to a narrow region of the polymer coating (≈200 μm wide) that is experiencing sufficiently high electrostatic forces to overcome the surface tension. We compared the size and shape of the jet and fiber diameters obtained from our method to those obtained by syringe and edge melt electrospinning. By inducing a concentrated electrostatic field near the polymer source, the size of the jet was reduced by nearly an order of magnitude, leading to over ≈75% reduction in the fiber diameter.

The continuum model of the electrostatic fields around the wire demonstrates the role of the concentration electrostatic fields in generating thinner jets and fibers. Using FEA modeling, we observed that the electrostatic field is heavily concentrated at the tip of the wire, where the Taylor cone is generated. While in the more traditional syringe electrospinning setup, the electrostatic field is concentrated near the walls of the syringe, the electric field at the tip of the wire reaches 60 times the average electrostatic field intensity, which explains why the formed Taylor cone is much smaller than in syringe melt electrospinning.

Supporting Information

Supporting Information is available from the Wiley Online Library or from the author.

Acknowledgements

The authors would like to thank the U.S. National Science Foundation (Grant CMMI-1538048) for funding this work. Additional thanks to Dr. Joseph Lowery of DuPont, Mr. Nikhil Mayadeo, and Dr. Terry Creasy of Texas A&M University, and Dr. Mohammad Saed of Texas Tech University for their helpful input. The authors also would like to acknowledge the support from TAMU AggiE_Challenge program, as well as students in the program, especially Logan C. Duran, Navira Alifa, Emily K. Nowlin, and Joshua M. Yu Tiamco.

Conflict of Interest

The authors declare no conflict of interest.

Keywords

electrostatic field gradient, melt electrospinning, nanofibers, Taylor cone, thermoplastics

Received: July 11, 2018
Revised: October 13, 2018
Published online: November 2, 2018

[1] Z. M. Huang, Y. Z. Zhang, M. Kotaki, S. Ramakrishna, *Compos. Sci. Technol.* **2003**, *63*, 2223.
[2] A. Podgórski, A. Bałazy, L. Gradoń, *Chem. Eng. Sci.* **2006**, *61*, 6804.
[3] L. Wang, Y. Yu, P. C. Chen, D. W. Zhang, C. H. Chen, *J. Power Sources* **2008**, *183*, 717.
[4] C. Kriegel, A. Arrechi, K. Kit, D. J. McClements, J. Weiss, *Crit. Rev. Food Sci. Nutr.* **2008**, *48*, 775.
[5] S. Khorshidi, A. Solouk, H. Mirzadeh, S. Mazinani, J. M. Lagaron, S. Sharifi, S. Ramakrishna, *J. Tissue Eng. Regener. Med.* **2016**, *10*, 715.
[6] G. Hochleitner, A. Youssef, A. Hrynevich, J. N. Haigh, T. Jungst, J. Groll, D. Dalton Paul, *Bio Nano Materials*, **2016**, *17*, 159.
[7] F. M. Wunner, M.-L. Wille, T. G. Noonan, O. Bas, P. D. Dalton, E. M. De-Juan-Pardo, D. W. Hutmacher, *Adv. Mater.* **2018**, *30*, 1706570.
[8] R. Ding, H. Wu, M. Thunga, N. Bowler, M. R. Kessler, *Carbon* **2016**, *100*, 126.
[9] M. Kim, Y. Kim, K. M. Lee, S. Y. Jeong, E. Lee, S. H. Baeck, S. E. Shim, *Carbon* **2016**, *99*, 607.
[10] S. Chawla, J. Cai, M. Naraghi, *Carbon* **2017**, *117*, 208.
[11] C. Huang, S. Chen, D. H. Reneker, C. Lai, H. Hou, *Adv. Mater.* **2006**, *18*, 668.
[12] V. Z. Mordkovich, *Theor. Found. Chem. Eng.* **2003**, *37*, 429.
[13] D. Papkov, Y. Zou, M. N. Andalib, A. Goponenko, S. Z. D. Cheng, Y. A. Dzenis, *ACS Nano* **2013**, *7*, 3324.
[14] S. R. Baker, S. Banerjee, K. Bonin, M. Guthold, *Mater. Sci. Eng., C* **2016**, *59*, 203.
[15] H. M. Pauly, D. J. Kelly, K. C. Popat, N. A. Trujillo, N. J. Dunne, H. O. McCarthy, T. L. Haut Donahue, *J. Mech. Behav. Biomed. Mater.* **2016**, *61*, 258.
[16] Z. Liu, R. Chen, J. He, *Mater. Des.* **2016**, *94*, 496.

[17] A. K. Higham, C. Tang, A. M. Landry, M. C. Pridgeon, E. M. Lee, A. L. Andrady, S. A. Khan, *AIChE J.* **2014**, *60*, 1355.
[18] H. R. Darrell, C. Iksoo, *Nanotechnology* **1996**, *7*, 216.
[19] J. D. Schiffman, C. L. Schauer, *Polym. Rev.* **2008**, *48*, 317.
[20] K-i. Tanaka, *Internationales Archiv für Arbeitsmedizin* **1971**, *28*, 95.
[21] P. de Haan, B. M. E. von Blomberg-van der Flier, J. de Groot, C. Nieboer, D. P. Bruynzeel, *Dermatology* **1994**, *188*, 126.
[22] J. W. Clayton, J. R. Barnes, D. B. Hood, G. W. H. Schepers, *Am. Ind. Hyg. Assoc. J.* **1963**, *24*, 144.
[23] J. Lyons, F. Ko, *Polym. News* **2005**, *30*, 170.
[24] J. Lyons, C. Li, F. Ko, *Polymer* **2004**, *45*, 7597.
[25] H. Gernot, J. Tomasz, D. B. Toby, H. Kathrin, M. Claus, J. Franz, D. D. Paul, G. Jürgen, *Biofabrication* **2015**, *7*, 035002.
[26] H. Chaobo, C. Shuiliang, L. Chuilin, H. R. Darrell, Q. Haiyan, Y. Ying, H. Haoqing, *Nanotechnology* **2006**, *17*, 1558.
[27] D. H. Reneker, A. L. Yarin, *Polymer* **2008**, *49*, 2387.
[28] F. M. Wunner, J. Maartens, O. Bas, K. Gottschalk, E. M. De-Juan-Pardo, D. W. Hutmacher, *Mater. Lett.* **2018**, *216*, 114.
[29] M. Castilho, D. Feyen, M. Flandes-Iparraguirre, G. Hochleitner, J. Groll, P. A. Doevendans, T. Vermonden, K. Ito, J. P. Sluijter, J. Malda, *Adv. Healthcare Mater.* **2017**, *6*, 1700311.
[30] A. Hrynevich, P. Dalton, J. Groll, J. N. Haigh, G. Hochleitner, B. Şen Elçi, Biofabric. Hierarch. In Vitro Tissue Models (Eds: J. Groll, J. Malda), Schloss Hernstein Hernstein, Austria, **2017**, http://dc.engconfintl.org/biofab_tissue_model/10.
[31] N. E. Zander, *J. Appl. Polym. Sci.* **2015**, *132*, n/a.
[32] R. G. Larson, P. S. Desai, *Annu. Rev. Fluid Mech.* **2015**, *47*, 47.
[33] R. Nayak, R. Padhye, I. L. Kyratzis, Y. B. Truong, L. Arnold, *Text. Res. J.* **2013**, *83*, 606.
[34] N. Mayadeo, K. Morikawa, M. Naraghi, M. J. Green, *J. Polym. Sci., Part B: Polym. Phys.* **2017**, *55*, 1393.
[35] E. Zhmayev, H. Zhou, Y. L. Joo, *J. Non-Newtonian Fluid Mech.* **2008**, *153*, 95.
[36] E. Zhmayev, D. Cho, Y. L. Joo, *Polymer* **2010**, *51*, 274.
[37] H. Zhou, T. B. Green, Y. L. Joo, *Polymer* **2006**, *47*, 7497.
[38] S. Maity, L. N. Downen, J. R. Bochinski, L. I. Clarke,*Polymer* **2011**, *52*, 1674.
[39] F. Ko, Y. Gogotsi, A. Ali, N. Naguib, H. Ye, G. L. Yang, C. Li, P. Willis, *Adv. Mater.* **2003**, *15*, 1161.
[40] P. Potschke, T. Villmow, B. Krause, *Polymer* **2013**, *54*, 3071.
[41] W. Qingqing, K. C. Colin, T. Nagarajan Muthuraman, R. B. Jason, E. G. Russell, I. C. Laura, *Mater. Res. Express* **2014**, *1*, 045304.
[42] N. M. Thoppey, J. R. Bochinski, L. I. Clarke, R. E. Gorga, *Nanotechnology* **2011**, *22*, 345301.
[43] D. W. Hutmacher, P. D. Dalton,*Chem. Asian J.* **2011**, *6*, 44.
[44] P. D. Dalton, D. Grafahrend, K. Klinkhammer, D. Klee, M. Möller, *Polymer* **2007**, *48*, 6823.
[45] E. Schäffer, T. Thurn-Albrecht, T. P. Russell, U. Steiner, *Nature* **2000**, *403*, 874.
[46] R. Verma, A. Sharma, K. Kargupta, J. Bhaumik, *Langmuir* **2005**, *21*, 3710.
[47] S. Koombhongse, W. Liu, D. H. Reneker, *J. Polym. Sci., Part B: Polym. Phys.* **2001**, *39*, 2598.
[48] J. M. Deitzel, J. Kleinmeyer, D. Harris, N. C. Beck Tan, c*Polymer* **2001**, *42*, 261.
[49] W. Wei, Z. Gu, S. Wang, Y. Zhang, K. Lei, K. Kase *J. Micromech. Microeng.* **2012**, *23*, 015004.
[50] B. Bogdanov, A. Vidts, A. Van Den Buicke, R. Verbeeck, E. Schacht, *Polymer* **1998**, *39*, 1631.
[51] A. Wurm, E. Zhuravlev, K. Eckstein, D. Jehnichen, D. Pospiech, R. Androsch, B. Wunderlich, C. Schick, *Macromolecules* **2012**, *45*, 3816.
[52] G. Zhu, Q. Xu, R. Qin, H. Yan, G. Liang, *Radiat. Phys. Chem.* **2005**, *74*, 42.
[53] J. E. K. Schawe. *J. Appl. Polym. Sci.* **2016**, *133*, 42977.